SPECIAL IPWG-7 COLLECTION

Improvements to the GOES-R Rainfall Rate Algorithm

ROBERT J. KULIGOWSKI

NOAA/NESDIS/Center for Satellite Applications and Research, College Park, Maryland

YAPING LI AND YAN HAO

I. M. Systems Group, Rockville, Maryland

YU ZHANG

NOAA/NWS/National Water Center, Silver Spring, Maryland

(Manuscript received 1 October 2015, in final form 29 January 2016)

ABSTRACT

The National Oceanic and Atmospheric Administration (NOAA) Geostationary Operational Environmental Satellite series R (GOES-R) will greatly expand the ability to observe the earth from geostationary orbit compared to the current-generation GOES, with more than 3 times as many spectral bands and a 75% reduction in footprint size. These enhanced capabilities are beneficial to rainfall rate estimation since they provide sensitivity to cloud-top properties such as phase and particle size that cannot be achieved using the limited channel selection of current GOES. The GOES-R rainfall rate algorithm, which is an infrared-based algorithm calibrated in real time against passive microwave rain rates, has been previously described in an algorithm theoretical basis document (ATBD); this paper describes modifications since the release of the ATBD, including a correction for evaporation of precipitation in dry regions and improved calibration updates. These improvements have been evaluated using a simplified version applicable to current-generation GOES to take advantage of the high-resolution ground validation data routinely available over the conterminous United States. Correcting for subcloud evaporation using relative humidity from a numerical model reduced false alarm rainfall by half and reduced the overall error by 35% for hourly accumulations validated against the National Centers for Environmental Prediction stage IV radar–gauge field; however, the number of missed events did increase slightly. Reducing the size of the calibration regions and increasing the training data requirements improved the consistency of the retrieved rates in time and space and reduced the overall error by an additional 4%.

1. Introduction

Rapid assessment of and response to flood and flash flood events is essential in order to reduce their threats to life and property. A central element to predicting these events is timely and high-resolution precipitation observations, which serve as the basis of both situational awareness and prediction. However, many parts of the world lack the observational infrastructure (e.g., telemetered gauges and weather radars) to obtain situational information in time to adequately warn the public. Even in parts of the United States, the lack of adequate radar coverage [particularly the western United States and outside the conterminous United States (CONUS)] hampers forecaster efforts to predict flash flooding (Zhang et al. 2013). Rainfall estimates from satellites can complement other sources of data with their low latency and complete spatial and temporal coverage.

Operational estimation of rainfall using satellite data at the National Oceanic and Atmospheric Administration (NOAA) began in the 1970s with the largely manual Interactive Flash Flood Analyzer (Scofield 1987), which was automated into the Autoestimator in the 1990s (Vicente et al. 1998, 2002) and then improved upon with the Hydroestimator (HE; Scofield and Kuligowski

Corresponding author address: Robert J. Kuligowski, NOAA/NESDIS/STAR/SMCD, NCWCP ERA2, 5830 University Research Court, 2nd Floor, Office #2828, College Park, MD 20740-3818.
E-mail: bob.kuligowski@noaa.gov

DOI: 10.1175/JHM-D-15-0186.1

© 2016 American Meteorological Society

2003). These estimates are available to National Weather Service (NWS) field offices via the Advanced Weather Interactive Processing System (AWIPS) and are processed within a few minutes of the satellite image being received on the ground. They have been proven highly valuable to NWS forecasters, such as those at the West Gulf River Forecast Center (WGRFC), who have been using them to supplement their rainfall estimates over northern Mexico for predicting the floods along the Rio Grande (G. Story, WGRFC, 2001, personal communication). In addition, the HE is produced for the entire globe equatorward of 65° latitude and is used in such efforts as the Global Flash Flood Guidance (GFFG) system developed by the Hydrologic Research Center (Georgakakos et al. 2013).

Of course, rainfall rate estimates based on passive microwave (PMW) data are also critically important, particularly since PMW radiances are sensitive to bulk cloud water or ice that is more strongly related to surface precipitation rates than infrared (IR) cloud-top brightness temperatures. These estimates are a core component of satellite and multisensor products that are used for climate analysis and other applications that can use data with longer latencies, such as the Climate Prediction Center (CPC) morphing technique (CMORPH; Joyce et al. 2004) and the National Aeronautics and Space Administration (NASA) Tropical Rainfall Measuring Mission (TRMM) Multisatellite Precipitation Analysis (TMPA; Huffman et al. 2007) and its replacement for the Global Precipitation Measurement (GPM) mission, the Integrated Multisatellite Retrievals for GPM (IMERG; Huffman et al. 2015). However, for analyzing rapidly evolving high-impact precipitation events in an operational forecasting environment, precipitation information needs to be available with very little delay and updated frequently (e.g., Zhang et al. 2013), and this has made it challenging to directly use PMW information in an operational environment. Consequently, despite the challenges of using IR data for estimating rainfall, it remains an important source of information for real-time forecasting applications.

As a legacy algorithm based on concepts from the 1970s [before water vapor imagery was available from the Geostationary Operational Environmental Satellite (GOES)] and required at night and not just during the day (precluding the use of visible data), the HE uses information from only the IR window channel at approximately 11 μm. The upcoming launch of GOES series R (GOES-R) will greatly increase the spectral capability of imaging from geostationary orbit over the Western Hemisphere, making 16 spectral bands in the visible and IR available on the Advanced Baseline Imager (ABI) compared to just five on the current GOES Imager, and also reducing the footprint in the IR from 4 to 2 km (Schmit et al. 2005).

To prepare for these capabilities, the GOES-R Algorithm Working Group (AWG) was tasked with selecting and demonstrating algorithms that would build upon legacy operational capabilities and expand them to the new imaging capabilities of the GOES-R ABI. The AWG evaluated several candidates that could potentially meet the strict latency requirements of the rainfall rate algorithm, including the CPC quick morphing technique (QMORPH), which is a version of CMORPH (Joyce et al. 2004) that relies only on advecting PMW rainfall rate images; Precipitation Estimation from Remotely Sensed Information Using Artificial Neural Networks (PERSIANN; Hsu et al. 1997); and the Naval Research Laboratory (NRL) algorithm (Turk et al. 2003). Using the Spinning Enhanced Visible and Infrared Imager (SEVIRI) on board *Meteosat-8* as a proxy for the GOES-R ABI inputs, the AWG evaluated these algorithms and decided to use a new version of the Self-Calibrating Multivariate Precipitation Retrieval (SCaMPR) algorithm (Kuligowski 2002; Kuligowski et al. 2013). As will be described in more detail in the next section, SCaMPR calibrates in real time the GOES rainfall rate estimates against rainfall rates retrieved from PMW instruments, and it uses statistical techniques to select the optimal predictors and coefficients for separately identifying rain areas and estimating rainfall rates.

It should be noted that algorithms that directly use PMW rain rates (e.g., CMORPH, TMPA, and IMERG) are more accurate than SCaMPR, which only uses PMW rain rates as a calibration standard. However, the latency requirement for the GOES-R rainfall rate algorithm (less than 5 min) precludes the direct use of PMW rain rates and thus sacrifices a degree of accuracy to achieve much lower latency (a few minutes, compared to roughly 18 h for CMORPH and 4 h for IMERG), though its accuracy is still sufficient for hydrologic forecasting in regions of sparse gauge coverage (Zhang et al. 2013; Lee et al. 2014). The performance of the GOES-R rainfall rate algorithm is also expected to be superior to that of the version of SCaMPR evaluated in these previously published papers because the additional spectral bands will improve sensitivity to cloud-top properties (e.g., phase and particle size) that will enable raining clouds to be more skillfully discriminated from nonraining clouds (e.g., Ba and Gruber 2001; Behrangi et al. 2009; Rosenfeld and Lensky 1998), in addition to the improvements described in this paper.

To prepare NWS forecasters and other users for this new capability, the algorithm developers created a simplified version of the algorithm that uses the limited

channel set of current GOES; since 2011 they have teamed with the NASA Short-Term Prediction Research and Transition Center (SPoRT) to make the rain rates available in real time to selected forecast offices for evaluation. The purpose of this paper is to describe the improvements to the algorithm that have resulted from the outcome of evaluations at the forecast offices. It will not serve as an evaluation of the full algorithm (only of the impact of the improvements) since the work described here uses a simplified version that can be readily validated at small scales in time and space with the finescale ground validation data available over the CONUS. The second section of this paper will briefly review the full GOES-R version of the algorithm as described in the algorithm theoretical basis document (ATBD; Kuligowski 2010) and note the differences from previous versions of the algorithm. The simplifications made to the algorithm to apply it to current-generation GOES images in real time will also be mentioned. Section 3 of this paper will describe the modifications that were made to the algorithm in response to forecaster feedback and will demonstrate the impact of those modifications on the simplified algorithm, which are expected to be similar to the impact they would have on the full algorithm. The paper will then close with a summary and a description of ongoing work to further improve the algorithm.

2. Basic algorithm description

a. GOES-R version

The GOES-R version of SCaMPR is described in detail in Kuligowski (2010) but will be outlined here for reference. Essentially, the intent of the algorithm is to use IR data from geostationary satellite platforms to replicate as closely as possible the characteristics of rainfall rates derived from PMW data from low-Earth-orbiting satellites, but for the full spatial and temporal coverage of GOES. To provide the best fit possible between the IR predictors and the target PMW rain rates, the relationships derived between the two are allowed to vary in time, in space, and by cloud type.

The starting point for this approach is a rolling-value dataset in which IR data from GOES are matched with and aggregated to the 8-km resolution of the target PMW rain rates, which are obtained from the CPC combined microwave (MWCOMB) dataset (Joyce et al. 2004). MWCOMB overlays all available PMW rain rates during a 30-min period and intercalibrates them so the distributions from each PMW sensor matches that of the rain rates from the GPM Microwave Imager [GMI; previously using the TRMM Microwave Imager (TMI) for this purpose]. It should be stressed that calibration against MWCOMB means that SCaMPR would be expected to exhibit some of the weaknesses of PMW rain rates (e.g., underestimation of rainfall in warm-top clouds); however, PMW rain rates are used as the calibration standard for other satellite rainfall algorithms as well (e.g., CMORPH and TMPA/IMERG) since they are the only source of instantaneous rain rates that are reliably available over most of the globe in real time.

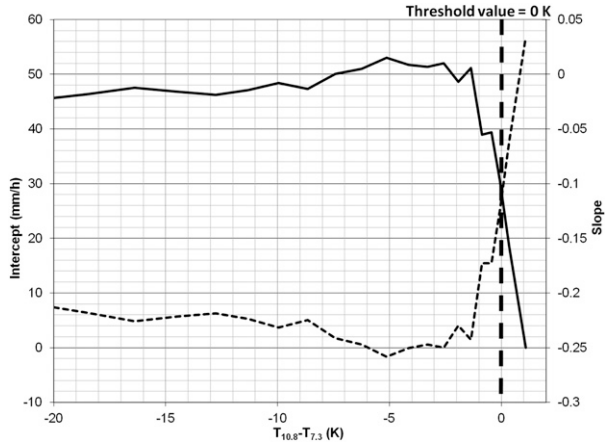

FIG. 1. Relationship between slope (solid line) and intercept (dashed) of the best-fit line between SEVIRI 10.8-μm brightness temperature and MWCOMB rain rates as a function of the brightness temperature difference between 10.8 and 7.3 μm.

To allow the calibration relationship to vary in space and by cloud type, separate matched PMW–IR datasets are kept for four 30° latitude bands (covering 60°S–60°N) and also for three different cloud types. These cloud types are not directly based on retrieved cloud properties but on observed changes in the relationship between the IR window brightness temperature and the PMW rain rate as a function of different GOES IR parameters. An example of this is shown in Fig. 1, which illustrates the transition in the slope and intercept of the best-fit line between 10.8 μm SEVIRI brightness temperature $T_{10.8}$ and MWCOMB rain rates as a function of the difference in brightness temperature between the 10.8- and 7.3-μm SEVIRI bands. The transition indicates a shift from stratiform and shallow convective clouds to deep convective clouds, because clouds with a higher brightness temperature in a water vapor band like 7.3 μm than in a window band like 10.8 μm appear to be deep convective clouds that have ejected water vapor into the stratosphere, producing a warm signal in the water vapor band (e.g., Fritz and Laszlo 1993; Schmetz et al. 1997; Tjemkes et al. 1997).

A similar analysis using the brightness temperature difference between the 8.5- and 10.8-μm SEVIRI bands

formed the basis for separating these non–deep convective clouds into two types: water-top clouds and ice-top clouds. The relative differences in emissivity of liquid water and ice at 8.5 and 10.8 μm mean that the difference in brightness temperature between these two bands can indicate cloud-top phase, with water-top clouds having lower $T_{8.5}$ relative to $T_{10.8}$ and the opposite being the case for ice-top clouds (Ackerman et al. 1990). The final result is three cloud types with the following thresholds (transposing the central wavelengths of each band from SEVIRI to the ABI): water-top clouds ($T_{7.34} < T_{11.2}$ and $T_{8.7} - T_{11.2} < -0.3$ K), ice-top clouds ($T_{7.34} < T_{11.2}$ and $T_{8.5} - T_{11.2} \geq -0.3$ K), and deep convective clouds ($T_{7.34} \geq T_{11.2}$). When combined with the four 30° latitude bands, this classification results in 12 rainfall classes.

It should be noted that this represents a change from the previously published version of SCaMPR in Kuligowski et al. (2013) that had no cloud classification. In addition, the Kuligowski et al. (2013) version of SCaMPR had more calibration regions (15° × 15° regions with 10° of overlap on each side) than the initial GOES-R version (Kuligowski 2010). Fewer calibration regions were used in the initial GOES-R version because at the time no significant benefit was demonstrated for the additional computational expense of smaller calibration regions; however, as will be shown in section 3b, this initial analysis later proved to be incorrect and so this decision was reversed based on additional evidence.

As with the previous version of SCaMPR (Kuligowski et al. 2013), the amount of training data required was based on a minimum number of raining MWCOMB pixels (defined as rates >1 mm h^{-1}) instead of a fixed time period to ensure greater consistency over time. Sensitivity studies were used to establish a minimum of 5000 pixels with rain rates >1 mm h^{-1} for the previously defined GOES-classified water-top and ice-top cloud types and at least 1000 for the deep convective cloud types. When new MWCOMB data become available, the oldest matched data are removed from the dataset to maintain the required number of pixels with rain rates >1 mm h^{-1}.

Whenever the rolling-value matched datasets for any rainfall class are updated, the calibration is updated in two steps: rain/no rain discrimination and rainfall rate calibration. Discriminant analysis is used to perform the former, first selecting the predictor that produces the highest Heidke skill score (HSS) when used to identify raining pixels, with a constraint requiring the resulting bias to be no more than 2%. This first predictor is then combined with all remaining predictors to identify the best predictor pair for rain/no rain discrimination.

TABLE 1. List of ABI predictors used by the GOES-R rainfall rate algorithm.

$T_{6.19} - 174$ K	$T_{8.5} - T_{7.34} + 30$ K
$S = 0.568 - (T_{\mathrm{min},11.2}) - 217$ K $+ 25$ K	$T_{11.2} - T_{7.34} + 20$ K
$T_{\mathrm{avg},11.2} - T_{\mathrm{min},11.2} - S + 85$ K	$T_{8.5} - T_{11.2} + 30$ K
$T_{7.34} - T_{6.19} + 30$ K	$T_{11.2} - T_{12.3} + 20$ K

Stepwise forward linear regression is then used to select the best two predictors for rainfall rate retrieval. Since the relationship between IR brightness temperatures and rainfall rates is highly nonlinear [e.g., Fig. 1a of Vicente et al. (1998)], as a preprocessing step each predictor is regressed against the MWCOMB rain rates in log–log space to produce additional nonlinear (power-law transform) predictors that are added to the pool of predictors. Prior to transformation to log space, predetermined constant values were added to some predictors (e.g., to brightness temperature differences between bands) to prevent negative values since the logarithm of a negative value is undefined. For other predictors (e.g., single-channel brightness temperature values), predetermined constant values were subtracted to reduce the values to close to (but still above) zero in order to optimize the nonlinear transformation.

The pool of available predictors was selected from all of the possible combinations of ABI bands relevant to rainfall rate retrieval: the two water vapor bands at 6.19 and 7.34 μm and the three IR window bands at 8.5, 11.2, and 12.0 μm. The resulting list was narrowed down to eight possible predictors based on how frequently they were selected (predictors selected only a few percent of the time or less were dropped), and the final list is shown (including the adjustments that were used to prevent negative numbers or keep the numbers positive but small) in Table 1. The second and third predictors in the left-hand column are measures of cloud texture (intended to discriminate cirrus from cumulus clouds) adapted from Adler and Negri (1988) and Ba and Gruber (2001): T_{avg} is the average value of $T_{11.2}$ computed over the 5 × 5 pixel area centered on the pixel, and T_{min} is the minimum temperature over the closest six neighboring pixels (four along the scan line and two across scans).

The mean-square-error minimization implicit in linear regression is problematic when applied to rainfall rates because it will optimize for extremely light rainfall rates since they represent the vast majority of the rainfall data; this results in very poor fits for the higher rainfall rates that are critical for flash flood forecasting. As a result, the distribution of the SCaMPR rain rates tends to be shifted far to the left (toward lower rainfall rates) relative to the calibration MWCOMB rain rates. SCaMPR adds a histogram matching step to address this

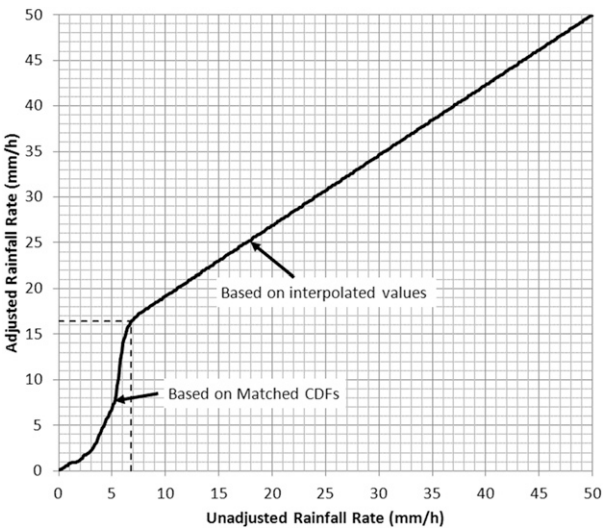

FIG. 2. Example of the LUT for adjusting the distribution of the SCaMPR rain rates to match the MWCOMB data. Annotations indicate those portions of the LUT derived using the matched CDFs of SCaMPR and MWCOMB and derived by interpolating between the highest value of the CDFs and matching values of 50 mm h^{-1}.

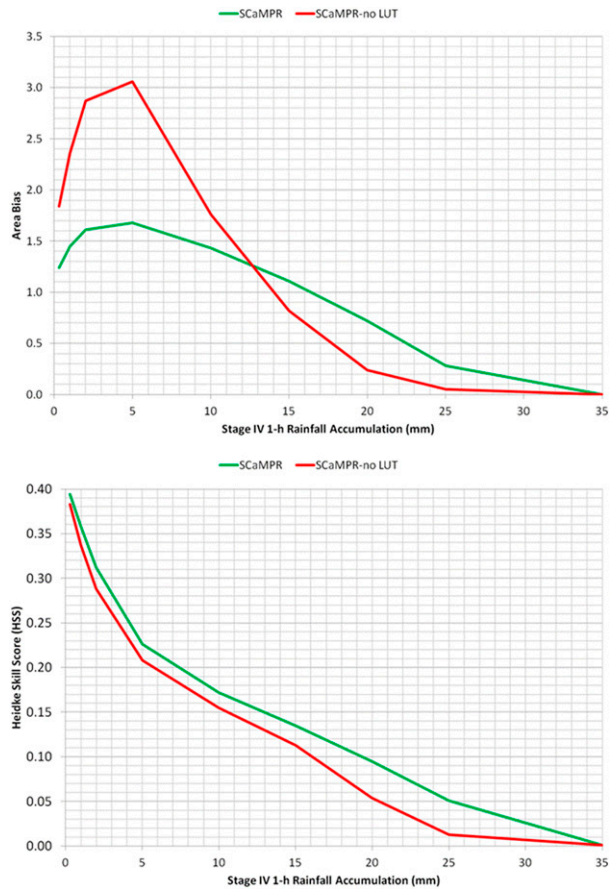

FIG. 3. Area (top) bias and (bottom) HSS of 1-h accumulations from the original current GOES version of the GOES-R rainfall rate algorithm with (green line) and without (red line) the distribution adjustment vs 1-h stage IV accumulations for July 2011.

issue; that is, a lookup table (LUT) is generated to map the cumulative distribution function (CDF) of the SCaMPR rain rates to that of the MWCOMB rain rates, producing an LUT that is applied to the SCaMPR rain rates to produce rain rates with a statistical distribution consistent with that of the target MWCOMB rain rates. To handle any retrieved rain rates that are higher than the maximum rain rate in the training data, the LUT is linearly interpolated from the highest value in the matched histograms to no adjustment at the highest MWCOMB rain rate of 50 mm h^{-1}; that is, the unadjusted and adjusted values are the same for rain rates $\geq$50 mm h^{-1}. This is done because extrapolation would run the risk of producing physically unreasonable results, as would be suggested by extrapolating the curved portion of the sample adjustment in Fig. 2. This is a significant change from the version of SCaMPR evaluated in Zhang et al. (2013) and addresses some of the problem of underestimated heavy rainfall and overestimated light rainfall pointed out in that paper, as illustrated by comparing the area bias and HSS for the algorithm applied to current GOES (see section 2b) for 1-h accumulations as a function of 1-h, 4-km NCEP stage IV gauge–radar rainfall accumulation (Lin and Mitchell 2005) during July 2011 (Fig. 3).

The resulting predictor lists and calibration coefficients for both rain and no rain discrimination and rainfall rate retrieval plus the adjustment LUTs are kept in a file that is used by SCaMPR to retrieve rain rates from the current GOES imagery. Data matching/calibration and retrieval are run in parallel so that the latency of the MWCOMB data (approximately 15 h) has no effect on the latency of the GOES retrievals, which is just minutes after the GOES data become available.

b. *Simplification for current GOES*

Although the algorithm was developed using SEVIRI data, the need for forecasters to evaluate the algorithm over the United States prior to the operational deployment of GOES-R made it necessary to develop a simplified version that could run using current GOES capabilities. Two primary changes were necessary: the water-top and ice-top cloud categories had to be combined (since there is no 8.5-μm band to differentiate them), thus reducing the number of classes from 12 to 8, and half the predictors were lost, since there is no 8.5-μm band or 12.3-μm band and since there is only one water vapor band on current GOES. The four remaining

TABLE 2. List of GOES Imager predictors used by the current GOES version of the GOES-R rainfall rate algorithm.

$T_{6.7} - 174\,\mathrm{K}$	$T_{\mathrm{avg},10.7} - T_{\mathrm{min},10.7} - S + 85\,\mathrm{K}$
$S = 0.568 - (T_{\mathrm{min},10.7}) - 217\,\mathrm{K} + 25\,\mathrm{K}$	$T_{10.7} - T_{6.7} + 20\,\mathrm{K}$

predictors (with the central wavelengths reflecting the current GOES Imager rather than ABI) are indicated in Table 2.

This version began running in real time on GOES-West and -East in August 2011, covering 60°S–60°N and 165°E–15°W, with files in Man–Computer Interactive Data Access System (McIDAS) area file format [available at ftp://ftp.star.nesdis.noaa.gov/pub/smcd/emb/bobk/SPoRT/ and in flat (real*4) binary format at ftp://ftp.star.nesdis.noaa.gov/pub/smcd/emb/bobk/SPoRT/Binary/]. At the request of SPoRT, the coverage area was extended to 70°N in November 2011 to provide coverage for much of Alaska. Since that time, SPoRT has provided training and real-time data access to forecast offices in Medford, Oregon; the Alaska region; and San Juan, Puerto Rico, and is extending the evaluation to the Pacific region. In response to forecaster feedback, several improvements were made to the algorithm that will be detailed next.

3. Algorithm modifications and impacts

a. Humidity correction

An issue that was identified both from forecaster feedback and developer evaluation was significant false alarm rainfall in dry regions, for example, in intermountain areas. This was shown in Kuligowski et al. (2013) for the previous version of SCaMPR as well and is caused largely by the evaporation of hydrometeors below cloud base, which cannot be directly detected using satellite imagery. To resolve this, a correction based on mean relative humidity (RH) values from the lowest (vertical) third of the National Centers for Environmental Prediction (NCEP) Global Forecast System (GFS) model domain was developed; this same RH value is used to adjust rain rates in the current operational HE algorithm (Scofield and Kuligowski 2003), but a new correction has been empirically derived here. This adjustment (which is static rather than time variant like the rainfall rate retrieval calibration) was based on a 5-yr (2009–13) dataset of hourly stage IV radar–gauge rainfall totals matched with instantaneous MWCOMB rain rates (the SCaMPR calibration target) and aggregated onto the 1/8° latitude–longitude grid used by MWCOMB. Although MWCOMB represents instantaneous rates and cannot be readily aggregated into 1-h totals because the individual PMW scans are typically several hours apart, it was used in place of 1-h totals from SCaMPR in order to produce a more robust RH correction that would not have to be redone every time a change to SCaMPR was made. This matched dataset included only data east of 105°W given the well-known limitations of radar in the western United States (e.g., Young et al. 2000). These matched data were then sorted in order of RH value and then divided into bins of equal sample size, and for each bin the average stage IV rainfall minus the average MWCOMB rain rate was computed. A linear regression fit to the resulting data points was used to derive the following rainfall rate (RR) additive humidity adjustment ($\mathrm{RR_{add}}$):

$$\mathrm{RR_{add}} = \mathrm{RR} + 0.115825[\max(\mathrm{RH}, 61)] - 10.7354, \quad (1)$$

where RH is in percent and any negative values are rounded up to zero.

The ratios of stage IV to MWCOMB for each bin were likewise used to derive a multiplicative humidity adjustment; however, the additive adjustment was shown to have higher skill than the multiplicative adjustment when applied to a test set of SCaMPR rain rates. After applying the additive adjustment, the resulting rain rates were then used to derive a multiplicative adjustment to be applied after the additive adjustment of Eq. (1), which increased the skill of SCaMPR further. The multiplicative adjustment $\mathrm{RR_{mult}}$ is as follows:

$$\mathrm{RR_{mult}} = \mathrm{RR_{add}}\{0.000\,112\,891[\max(\mathrm{RH}, 22.32)]^2 - 0.005\,040\,12[\max(\mathrm{RH}, 22.32)] + 0.476\,117\}. \quad (2)$$

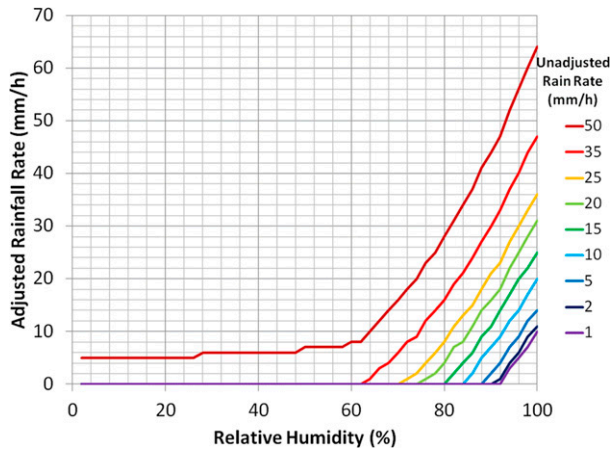

FIG. 4. SCaMPR RH correction as a function of GFS RH for different rain rates (mm h^{-1}; scale on right).

Figure 4 shows the resulting correction as a function of RH for different rainfall intensities; the correction is

TABLE 3. Performance statistics for 1-h SCaMPR accumulations without and with the RH correction compared to the operational HE algorithm, PERSIANN-CCS, and QMORPH for 2011–13.

Algorithm	Bias	RMSE	CC	To_{hit}	To_{miss}	To_{false}	To_{err}
HE	1.377	1.023	0.344	−0.030	0.318	0.694	0.982
SCaMPR	2.448	1.257	0.359	−0.384	0.319	1.400	1.335
SCaMPR-RH	1.183	0.894	0.375	−0.073	0.401	0.527	0.855
PERSIANN	1.249	1.016	0.260	−0.020	0.534	0.784	1.299
QMORPH	1.131	1.064	0.287	−0.126	0.493	0.518	0.884

quite strong in dry air, such that for an RH below 60% only the most intense cloud-level rainfall is assumed to reach the surface.

For a reanalyzed dataset covering all of 2011–13, the impact of the RH correction on SCaMPR skill (compared to 1-h stage IV amounts on a 4-km grid) is shown in Table 3, including a comparison to the current operational HE algorithm and to the PERSIANN–Cloud Classification System (PERSIANN-CCS; Mahrooghy et al. 2012) and QMORPH algorithms. The significant wet multiplicative volume bias (bias in Table 3) of SCaMPR is reduced by over half (from 2.448 to 1.183) and is brought below that of the HE. This reduction in bias also reduces the RMSE by nearly 29% compared to the original version and by over 10% compared to HE, PERSIANN-CCS, and QMORPH. The correlation between satellite estimates and hourly observations (CC in Table 3) improves slightly as well and is superior to the HE and significantly better than PERSIANN-CCS and QMORPH.

Following Tian et al. (2009), the total bias To_{err} (Table 3) can be computed as the total volume of satellite rainfall minus the total volume of stage IV rainfall and can be broken down into three components: the volume difference for pixels where SCaMPR and stage IV both had rainfall To_{hit} (with the rain/no rain threshold defined here as $0.25\,\mathrm{mm\,h^{-1}}$); the volume of rainfall for pixels where stage IV had rainfall and SCaMPR did not To_{miss}; and the volume difference when the opposite occurred, that is, false alarms To_{false}. These error components are related to the total error as follows:

$$To_{err} = To_{hit} - To_{miss} + To_{false}\,. \tag{3}$$

All of the rain volumes are normalized by dividing by the total volume of observed rainfall. As expected, the volume of false alarm rainfall is cut by nearly two-thirds by the humidity correction, though there is some increase in missed rainfall that is less than 10% of the magnitude of the reduction in false alarms. This reduction in false alarms reduces the volume of false alarm rainfall below that of every other algorithm except QMORPH (which is less than 2% better) and the missed rainfall, while 26% greater than that of the HE, is still significantly less than that of PERSIANN-CCS and QMORPH.

Interestingly, the additive volume bias in the "hit" pixels becomes less negative, which at first appears counterintuitive since the humidity correction generally reduces rainfall (with the exception of RH values near 100%). The apparent reason for this is that the RH correction completely removed the rainfall from some of the hit pixels that had previously been too dry already, causing them to be reclassified as "miss" and raising the average of the remaining hit pixels. However, this increase was still much smaller than the reduction in false alarms, and so the overall error was reduced by approximately 35% and is significantly lower than that of the other algorithms (though only about 3% lower than for QMORPH).

The effectiveness of the RH correction at reducing false alarms is illustrated in Fig. 5, which shows the spatial distribution of the normalized false alarm rainfall versus 4-km hourly stage IV for each 1° × 1° latitude–longitude box for the 6 years spanning 2008–13. False alarms are reduced everywhere, most notably in the high plains and the southwestern desert. Note that this figure does not include stage IV data from Northwest River Forecast Center (NWRFC) or California–Nevada River Forecast Center (CNRFC) since neither one produces routine hourly radar–gauge rainfall estimates. To examine these areas, the analysis was repeated for the same time period but comparing 24-h SCaMPR totals with daily Cooperative Observer Program (COOP) gauge amounts (Fig. 6). The magnitudes differ somewhat from Fig. 5 but the overall pattern is the same, with the greatest reductions in false alarms over the southwestern quarter of the CONUS but with reductions everywhere.

It should be noted that this RH correction has been derived and validated using only the eastern half of the CONUS, so it is not definitively known whether this correction is equally appropriate for the remainder of the GOES coverage area. Evaluation using reliable rainfall rate estimates outside the CONUS [e.g., from GPM Dual-Frequency Precipitation Radar (DPR)] will

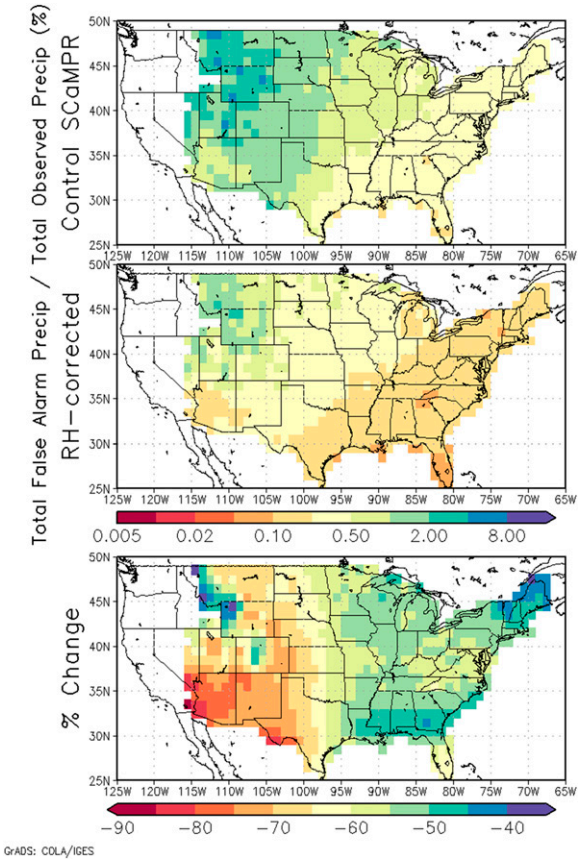

FIG. 5. Volume of false alarm rainfall divided by the volume of observed rainfall (compared to stage IV) during 2008–13 for (top) the original simplified GOES-R version of SCaMPR, with (middle) the RH correction applied and (bottom) the percentage change in false alarms from applying the RH correction. Gray shading indicates no data in the (top) and (middle); white indicates no data in the (bottom).

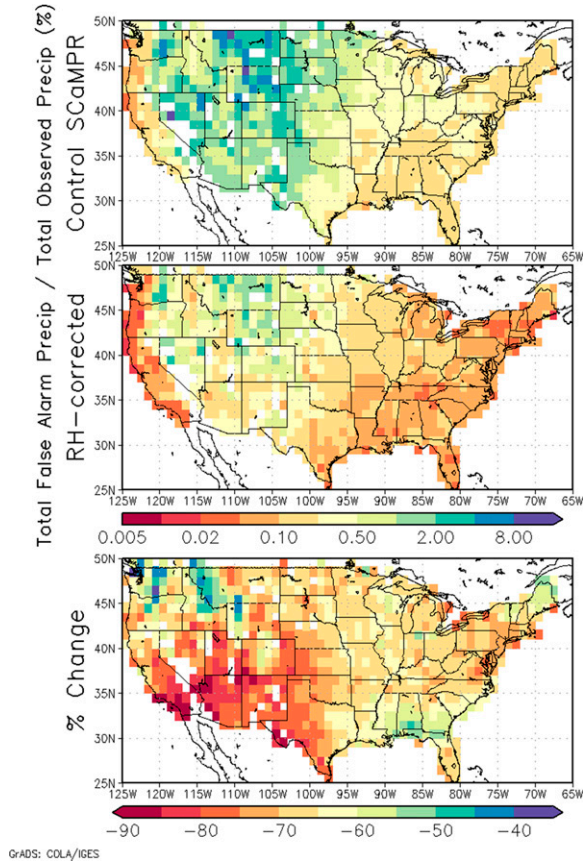

FIG. 6. As in Fig. 4, but for 24-h rainfall totals compared to gauges.

be needed to make this determination. In the meantime, this humidity adjustment was incorporated into the real-time processing in April 2014.

b. *Smaller calibration regions*

The NWS forecasters evaluating SCaMPR observed that the rainfall rates would occasionally show significant changes when the calibration was updated. This indicated that while the amount of calibration data was sufficient to ensure gradual calibration changes in most cases, there were occasions where a larger calibration dataset would be needed to assure a smoother transition when the calibration was updated.

In addition, forecasters noted that there were occasionally significant spatial discontinuities between the rainfall rates from the deep convective regions and those from the other raining pixels—areas of very high rain rates directly adjacent to pixels with zero rainfall, with no transition in between. Investigation revealed that the problem was also caused in part by the calibration datasets being too small, but another contributing factor was the application of histogram matching over such large calibration regions. Histogram matching neglects spatial information (i.e., the *n*th-highest unadjusted SCaMPR rain rate is matched with the *n*th-highest MWCOMB rain rate regardless of location), meaning that the LUT could be based on matches of SCaMPR and MWCOMB pixels belonging to completely different precipitation systems thousands of miles apart with no physical connection. Even given the commonality of precipitation physics for similar cloud types, this could result in significant nonphysical changes in the LUT from one hour to the next, for example, if the highest SCaMPR rain rate is associated with a growing thunderstorm and the highest MWCOMB rain rate is associated with a decaying one. It could also cause significant nonphysical differences in the LUTs of different rainfall types at different times for the same reasons. Since other applications of this approach (e.g., Turk et al. 2003; Huffman et al. 2007) use much smaller calibration regions than the 30° × 120° used in SCaMPR, nonoverlapping

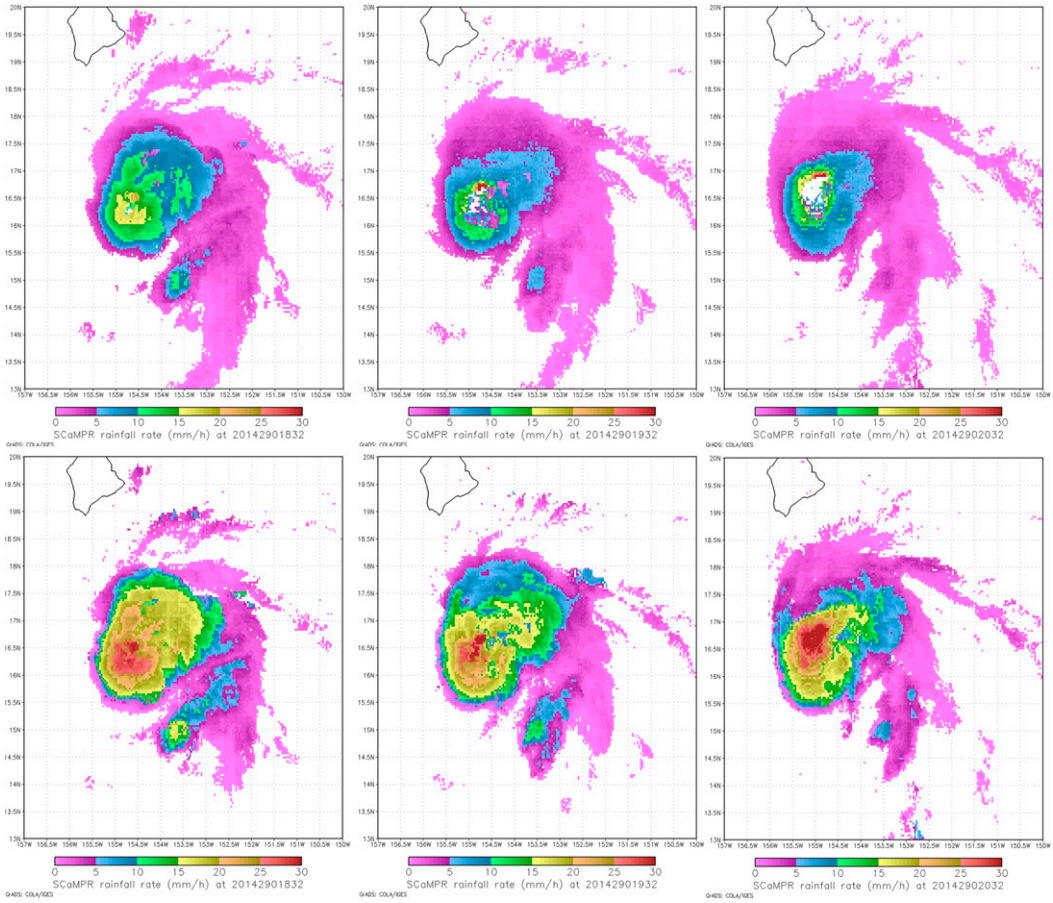

FIG. 7. SCaMPR rain rates for Tropical Storm Ana at (left) 1832, (center) 1932, and (right) 2032 UTC 17 Oct 2014 for (top) the original simplified GOES-R version of SCaMPR and (bottom) the modified version with smaller calibration regions.

calibration regions with sizes of 5° × 5°, 10° × 10°, and 15° × 15° were tested, with varying amounts of training data required. The 15° × 15° regions were found to address most of these issues when accompanied by a significant increase in the amount of training data to 10 000 pixels with rain rates $\geq 2.5\,\mathrm{mm\,h^{-1}}$ for both classes; smaller regions and/or larger amounts of training data did not have a significant positive impact, especially compared to the additional computational cost required. Of course, 15° × 15° calibration regions will create the possibility of long periods without significant rainfall in a particular region. In such a case, the calibration dataset and the calibration coefficients will remain static until new precipitation occurs and begins to refresh the calibration dataset. Differences in the rain/no rain and rainfall rate predictors and coefficients and/or in the histogram adjustments between adjacent 15° × 15° calibration regions can produce discontinuities along the boundary between the regions. Consequently, nine separate rainfall rates are retrieved for each pixel using the calibration from the region containing that pixel and also for the eight neighboring 15° × 15° regions; these nine values are then averaged using an inverse distance weighting scheme to produce smooth transitions at the interregion boundaries.

The impact of the change is illustrated in Fig. 7, which shows successive images from Tropical Storm Ana on 17 October 2014 (a reprocessed test case) as it approached the Hawaiian Islands. The enhancement of rainfall in the deep convective area can be clearly seen [note the large area of no rainfall near the storm center in Fig. 7 (top), which appears to be too temporally and spatially incoherent to be a real eye feature], along with the improved continuity from one hour to the next.

Statistically, the use of these regions also further improved performance, as shown in Table 4. The multiplicative volume bias actually falls below 0.9 (i.e., the rain volume is now 10% too low), and the RMSE declines another 9% and is now roughly 20% lower than that of HE, PERSIANN-CCS, and QMORPH. The

TABLE 4. Performance statistics for RH-corrected SCaMPR with the original calibration regions and with the smaller 15 × 15 calibration regions (15 × 15RH) compared to the operational HE algorithm, PERSIANN-CCS, and QMORPH for 2011–13.

Algorithm	Bias	RMSE	CC	To_{hit}	To_{miss}	To_{false}	To_{err}
HE	1.377	1.023	0.344	−0.030	0.318	0.694	0.982
SCaMPR-RH	1.183	0.894	0.375	−0.073	0.401	0.527	0.855
15 × 15RH	0.894	0.839	0.380	0.002	0.451	0.365	0.817
PERSIANN	1.249	1.016	0.260	−0.020	0.534	0.784	1.299
QMORPH	1.131	1.064	0.287	−0.126	0.493	0.518	0.884

correlation coefficient also has improved further. Regarding the error components, false alarms decrease by another 30% and the hit bias is nearly zero. Missed rainfall volume does increase by 12%, which puts it significantly above HE but still below PERSIANN-CCS and QMORPH, but the overall error is still slightly lower than in the original GOES-R version with only eight calibration classes (using current GOES) and significantly lower than that of the HE, PERSIANN-CCS, and QMORPH. These changes were integrated into the real-time current GOES version of the algorithm in August 2015.

4. Conclusions and future work

In this paper, the GOES-R rainfall rate algorithm has been described, along with improvements that have been made in response to forecaster feedback. The impact of these improvements has been demonstrated on a simplified version of the algorithm applied to current GOES that allows validation using the high-resolution stage IV radar–gauge dataset. Adding a correction for subcloud evaporation based on GFS model RH significantly reduced false alarm rainfall (though at the cost of some additional missed events). Reducing the size of the calibration regions and increasing the training data requirements improved the temporal continuity of the rain rates and also improved the consistency of the rain rates between the deep convective and non–deep convective clouds.

However, significant work remains to be done. One important item will be to refine the RH correction further: while it does significantly reduce false alarm rainfall and enhance skill for light rain rates, it has been found to degrade the performance of the algorithm for heavier rain rates by inducing a strong systematic dry bias (Fig. 8) that erases its advantage over HE, PERSIANN, and QMORPH at higher rain rates. This version of the RH correction is currently used in the real-time version of the algorithm, but work is underway to improve the correction by making it a function of both rainfall rate and RH; presumably, it would be relaxed for heavier rain rates relative to what is indicated by Fig. 4.

Another area for improvement is the detection of rainfall from warm clouds, which is challenging—significant rainfall is frequently observed in places like Hawaii and Puerto Rico from clouds with brightness temperatures above 273 K. The PMW rain rates from MWCOMB also frequently miss these events, so in such instances a fixed calibration may be necessary in lieu of the dynamic calibration against MWCOMB. However, cloud-top temperatures alone are not sufficient to discriminate raining warm

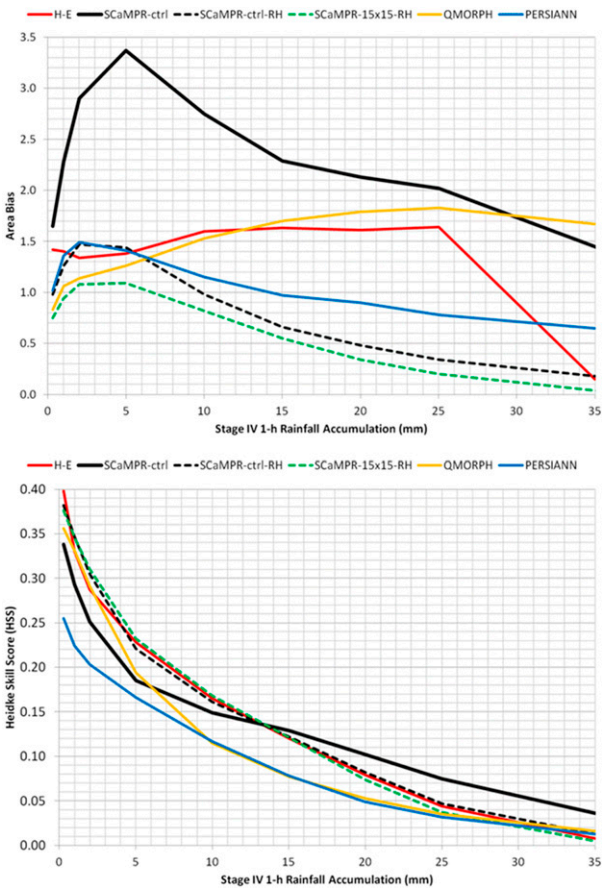

FIG. 8. Area (top) bias and (bottom) HSS of 1-h accumulations from the original current GOES version of the GOES-R rainfall rate algorithm, the algorithm with the RH correction added, and with the 15° × 15° calibration regions and the RH correction vs 1-h stage IV accumulations for 2008–13.

clouds from nonraining warm clouds, so work is underway to leverage efforts by Chen et al. (2011) to utilize cloud property information that is produced in real time at the University of Wisconsin using the daytime cloud optical and microphysical properties (DCOMP) algorithm (Walther and Heidinger 2012) and to identify a priori those conditions under which this cloud property information should be used in lieu of the dynamic calibration so that the choice of calibration can be fully automated. This information has also been demonstrated to be helpful in screening out cirrus anvils (Stenz et al. 2014)—another area for improvement identified by forecasters.

Orographic rainfall is another challenge raised by forecasters. Although the HE uses a basic orographic correction (Vicente et al. 2002), validation of the correction has produced less than satisfying results (Yucel et al. 2011) and efforts have been ongoing to develop a more robust orographic correction. However, the sheer complexity of orographic precipitation processes makes this an extremely challenging task.

Acknowledgments. This work was supported by the GOES-R Program Office and by the NOAA Office of Atmospheric Research (OAR) Earth System Research Laboratory (ESRL) U.S. Weather Research Program (USWRP). MWCOMB and QMORPH data and daily COOP gauge data were obtained from CPC via anonymous ftp; PERSIANN-CCS data were obtained from the University of California, Irvine, via anonymous ftp. Archive stage IV data were obtained from the University Corporation for Atmospheric Research (UCAR)/National Corporation for Atmospheric Research (NCAR) Computing, Data, and Software Facility (CDS). Archive GOES data were obtained from the University of Wisconsin Space Science and Engineering Center (SSEC). Figures 5–7 were created using the Grid Analysis and Display System (GrADS). The contents of this paper are solely the opinions of the authors and do not constitute a statement of policy, decision, or position on behalf of NOAA or the U.S. Government.

REFERENCES

Ackerman, S. A., W. L. Smith, J. D. Spinhirne, and H. E. Revercomb, 1990: The 27–28 October 1986 FIRE IFO cirrus case study: Spectral properties of cirrus clouds in the 8–12 m window. *Mon. Wea. Rev.*, **118**, 2377–2388, doi:10.1175/1520-0493(1990)118<2377:TOFICC>2.0.CO;2.

Adler, R. F., and A. J. Negri, 1988: A satellite infrared technique to estimate tropical convective and stratiform rainfall. *J. Appl. Meteor.*, **27**, 30–51, doi:10.1175/1520-0450(1988)027<0030:ASITTE>2.0.CO;2.

Ba, M. B., and A. Gruber, 2001: GOES multispectral rainfall algorithm (GMSRA). *J. Appl. Meteor.*, **40**, 1500–1514, doi:10.1175/1520-0450(2001)040<1500:GMRAG>2.0.CO;2.

Behrangi, A., K.-L. Hsu, B. Imam, S. Sorooshian, G. J. Huffman, and R. J. Kuligowski, 2009: PERSIANN-MSA: A precipitation estimation method from satellite-based multispectral analysis. *J. Hydrometeor.*, **10**, 1414–1429, doi:10.1175/2009JHM1139.1.

Chen, R., Z. Li, R. J. Kuligowski, R. Ferraro, and F. Weng, 2011: A study of warm rain detection using A-Train satellite data. *Geophys. Res. Lett.*, **38**, L04804, doi:10.1029/2010GL046217.

Fritz, S., and I. Laszlo, 1993: Detection of water vapor in the stratosphere over very high clouds in the tropics. *J. Geophys. Res.*, **98**, 22 959–22 967, doi:10.1029/93JD01617.

Georgakakos, K. P., R. Graham, R. Jubach, T. M. Modrick, E. Shamir, C. Spencer, and J. A. Sperfslage, 2013: Global Flash Flood Guidance System, phase I. HRC Tech. Rep. 9, Hydrologic Research Center, 134 pp. [Available online at http://www.hrc-lab.org/projects/projectpdfs/HRC%20Technical%20Report%20No%209.pdf.]

Hsu, K.-L., X. Gao, S. Sorooshian, and H. V. Gupta, 1997: Precipitation Estimation from Remotely Sensed Information Using Artificial Neural Networks. *J. Appl. Meteor.*, **36**, 1176–1190, doi:10.1175/1520-0450(1997)036<1176:PEFRSI>2.0.CO;2.

Huffman, G. J., and Coauthors, 2007: The TRMM Multisatellite Precipitation Analysis (TMPA): Quasi-global, multiyear, combined-sensor precipitation estimates at fine scales. *J. Hydrometeor.*, **8**, 38–55, doi:10.1175/JHM560.1.

——, D. T. Bolvin, D. Braithwaite, K. Hsu, R. Joyce, C. Kidd, E. J. Nelkin, and P. Xie, 2015: NASA Global Precipitation Measurement Integrated Multi-satellitE Retrievals for GPM (IMERG). Algorithm Theoretical Basis Doc., version 4.5, 30 pp. [Available online at http://pmm.nasa.gov/sites/default/files/document_files/IMERG_ATBD_V4.5_0.pdf.]

Joyce, R. J., J. E. Janowiak, P. A. Arkin, and P. Xie, 2004: CMORPH: A method that produces global precipitation estimates from passive microwave and infrared data at high spatial and temporal resolution. *J. Hydrometeor.*, **5**, 487–503, doi:10.1175/1525-7541(2004)005<0487:CAMTPG>2.0.CO;2.

Kuligowski, R. J., 2002: A self-calibrating real-time GOES rainfall algorithm for short-term rainfall estimates. *J. Hydrometeor.*, **3**, 112–130, doi:10.1175/1525-7541(2002)003<0112:ASCRTG>2.0.CO;2.

——, 2010: GOES-R Advanced Baseline Imager (ABI) Algorithm Theoretical Basis Document for Rainfall Rate (QPE). NOAA/NESDIS/STAR Algorithm Theoretical Basis Doc., version 2.0, 44 pp. [Available online at http://www.goes-r.gov/products/ATBDs/baseline/Hydro_RRQPE_v2.0_no_color.pdf.]

——, Y. Li, and Y. Zhang, 2013: Impact of TRMM data on a low-latency, high-resolution precipitation algorithm for flash-flood forecasting. *J. Appl. Meteor. Climatol.*, **52**, 1379–1393, doi:10.1175/JAMC-D-12-0107.1.

Lee, H., Y. Zhang, D.-J. Seo, R. J. Kuligowski, D. Kitzmiller, and R. Corby, 2014: Utility of SCaMPR satellite versus ground-based quantitative precipitation estimates in operational flood forecasting: The effects of TRMM data ingest. *J. Hydrometeor.*, **15**, 1051–1069, doi:10.1175/JHM-D-12-0151.1.

Lin, Y., and K. E. Mitchell, 2005: The NCEP stage II/IV hourly precipitation analyses: Development and applications. Preprints, *19th Conf. on Hydrology*, San Diego, CA, Amer. Meteor. Soc., 1.2. [Available online at https://ams.confex.com/ams/pdfpapers/83847.pdf.]

Mahrooghy, M., V. G. Anatharaj, N. H. Younan, J. Aanstoos, and K.-L. Hsu, 2012: On an enhanced PERSIANN-CCS algorithm for precipitation estimation. *J. Atmos. Oceanic Technol.*, **29**, 922–932, doi:10.1175/JTECH-D-11-00146.1.

Rosenfeld, D., and I. M. Lensky, 1998: Satellite-based insights into precipitation formation processes in continental and maritime convective clouds. *Bull. Amer. Meteor. Soc.*, **79**, 2457–2476, doi:10.1175/1520-0477(1998)079<2457:SBIIPF>2.0.CO;2.

Schmetz, J., S. A. Tjemkes, M. Gube, and L. van de Berg, 1997: Monitoring deep convection and convective overshooting with Meteosat. *Adv. Space Res.*, **19**, 433–441, doi:10.1016/S0273-1177(97)00051-3.

Schmit, T. J., M. M. Gunshor, W. P. Menzel, J. J. Gurka, J. Li, and A. S. Bachmeier, 2005: Introducing the next-generation Advanced Baseline Imager on GOES-R. *Bull. Amer. Meteor. Soc.*, **86**, 1079–1096, doi:10.1175/BAMS-86-8-1079.

Scofield, R. A., 1987: The NESDIS operational convective precipitation estimation technique. *Mon. Wea. Rev.*, **115**, 1773–1792, doi:10.1175/1520-0493(1987)115<1773:TNOCPE>2.0.CO;2.

——, and R. J. Kuligowski, 2003: Status and outlook of operational satellite precipitation algorithms for extreme precipitation events. *Wea. Forecasting*, **18**, 1037–1051, doi:10.1175/1520-0434(2003)018<1037:SAOOOS>2.0.CO;2.

Stenz, R., X. Dong, B. Xi, and R. J. Kuligowski, 2014: Assessment of SCaMPR and NEXRAD Q3 precipitation estimates using Oklahoma Mesonet observations. *J. Hydrometeor.*, **15**, 2484–2500, doi:10.1175/JHM-D-13-0199.1.

Tian, Y., and Coauthors, 2009: Component analysis of errors in satellite-based precipitation estimates. *J. Geophys. Res.*, **114**, D24101, doi:10.1029/2009JD011949.

Tjemkes, S. A., L. van de Berg, and J. Schmetz, 1997: Warm water vapor pixels over high clouds as observed by Meteosat. *Beitr. Phys. Atmos.*, **70**, 15–21.

Turk, F. J., E. E. Ebert, H. J. Oh, B.-J. Sohn, V. Levizzani, E. A. Smith, and R. Ferraro, 2003: Validation of an operational global precipitation analysis at short time scales. Preprints, *3rd Conf. on Artificial Intelligence*, Long Beach, CA, Amer. Meteor. Soc., JP1.2. [Available online at https://ams.confex.com/ams/pdfpapers/56865.pdf.]

Vicente, G. A., R. Scofield, and W. P. Menzel, 1998: The operational GOES infrared rainfall estimation technique. *Bull. Amer. Meteor. Soc.*, **79**, 1883–1898, doi:10.1175/1520-0477(1998)079<1883:TOGIRE>2.0.CO;2.

——, J. C. Davenport, and R. A. Scofield, 2002: The role of orographic and parallax corrections on real time high resolution satellite rain rate distribution. *Int. J. Remote Sens.*, **23**, 221–230, doi:10.1080/01431160010006935.

Walther, A., and A. K. Heidinger, 2012: Implementation of the daytime cloud optical and microphysical properties algorithm (DCOMP) in PATMOS-x. *J. Appl. Meteor. Climatol.*, **51**, 1371–1390, doi:10.1175/JAMC-D-11-0108.1.

Young, C. B., A. A. Bradley, W. F. Krajewski, and A. Kruger, 2000: Evaluating NEXRAD multisensor precipitation estimates for operational hydrologic forecasting. *J. Hydrometeor.*, **1**, 241–254, doi:10.1175/1525-7541(2000)001<0241:ENMPEF>2.0.CO;2.

Yucel, I., R. J. Kuligowski, and D. J. Gochis, 2011: Evaluating the hydro-estimator satellite rainfall algorithm over a mountainous region. *Int. J. Remote Sens.*, **32**, 7315–7342, doi:10.1080/01431161.2010.523028.

Zhang, Y., D.-J. Seo, D. Kitzmiller, H. Lee, R. J. Kuligowski, D. Kim, and C. Kondragunta, 2013: Comparative strengths of SCaMPR satellite QPEs with and without TRMM ingest versus gridded gauge-only analyses. *J. Hydrometeor.*, **14**, 153–170, doi:10.1175/JHM-D-12-053.1.